pp 1337–1357.
doi:10.1017/aer.2021.30

Adaptive sliding mode formation control for multiple flight vehicles with considering autopilot dynamic

W. Li, **Q. Wen and H. Zhou**
lion_lee1994@126.com
School of Aerospace Engineering
Beijing Institute of Technology
Beijing 100081
China

ABSTRACT

This paper mainly focuses on the cooperative control of formation configuration for multiple flight vehicles in the three-dimensional space. Considering the external disturbance of the system, the adaptive non-singular terminal sliding mode control law (NTSMC) is designed based on the virtual leader-follower method, which aims to ensure that each flight vehicle reaches the expected terminal position in a limited time and meet the configuration constraints. Further considering the first-order dynamic characteristic of the autopilot, a novel second-order sliding mode control (SOSMC) law is deduced with using the estimated information of sliding mode disturbance observer. The proposed control method ensures that all flight vehicles form the required space formation configuration simultaneously at a pre-designed time, and the chattering phenomenon of the sliding mode surface and acceleration response that nears the equilibrium point is effectively weaken. The stability of the proposed control law is verified by theoretical analysis and lots of mathematical simulations. The results show that the control algorithm in this paper can be used to guidance the formation controller design of multiple flight vehicles in the mid-guidance phase to some extent, and thus the cooperative flight stability of the system can be effectively improved.

Keywords: multiple flight vehicles; space formation configuration; virtual leader-follower; cooperative control; finite time convergent; chattering suppression

Received 4 January 2021; revised 10 March 2021; accepted 15 March 2021.

NOMENCLATURE

h	flight height
R	distance between the formation system and the target
L	distance between sub-vehicles
F	distances between the 1th flight vehicle m_1 and the other three ones
$\boldsymbol{x_{s,i}}$	position vector
$\boldsymbol{v_{s,i}}$	velocity vector
$\boldsymbol{a_{s,i}}$	acceleration command vector
$\boldsymbol{d_s}$	external disturbance
$\boldsymbol{x_{q,i}}$	expected position vector in the LOS coordinate system
$\boldsymbol{v_{q,i}}$	expected velocity vector in the LOS coordinate system
L_{23}, L_{24}, L_{34}	baseline length between each sub-vehicle
L_0	distance between the 1th sub-vehicle and the plane $T_2T_3T_4$
$\Delta center$	offset angle
$\boldsymbol{e_{1,i}}, \boldsymbol{e_{2,i}}$	position error vector and velocity error vector
$\boldsymbol{s}, \boldsymbol{s}_1, \boldsymbol{s}_2$	sliding mode surfaces
β, γ	sliding mode parameters
k_1, k_2, ρ, η	control law gains
$\boldsymbol{a_s}$	non-singular terminal sliding mode control law
$\delta, \hat{\delta}$	upper limit and estimate of disturbance
ε_1	small normal number
$\boldsymbol{V}, \boldsymbol{V}_1, \boldsymbol{V}_2$	lyapunov functions
T_{reach}	reach time
τ	delay time constant of autopilot
$\boldsymbol{a_{m,i}}$	the acceleration vector in the LOS coordinate system
k_0	control parameter
t_r	desired time
$\boldsymbol{z_0}, \boldsymbol{z_1}, \boldsymbol{z_2}$	estimations of disturbance observer
$\lambda_0, \lambda_1, \lambda_2$	observer gains

1.0 INTRODUCTION

The complex battlefield environment and the development of integrated anti-missile defense technology make the attack mode of single flight vehicle severely challenged; thus the cluster cooperative operation system is being introduced into future war[1–3]. The collaborative operation of multiple flight vehicles means that all members are formed into a combat network to conduct the real-time information interaction through a data link, so as to improve the anti-interference ability of the formation system and enlarge the cooperative detection probability to the target during the mid-guidance stage[3]. After entering the terminal guidance stage, the collaborative system can realise the saturation attack on the target[4]. For advanced reentry vehicles equipped with radar detector, which have high flight speed and wide flight airspace. For this kind of flight vehicle, such as anti-ship missile with radar seeker, they gain the target

https://doi.org/10.1017/aer.2021.30 Published online by Cambridge University Press

information using own sensor or leader's sensor in the cooperative case and then fly to the target relying on guidance command. In order to ensure the high-precision co-positioning of the target after the detectors are turned on, it is necessary for all flight vehicles to pull apart the required space distance and angle during the mid-guidance stage and then adjust the attitude of the projectile body to align the target.

As an important part in the process of cooperative combat, the formation flight control of multiple flight vehicles has attracted the attention of scholars. The formation technology of multiple flight vehicles was firstly applied to the under-actuated mechanical system such as spacecraft and UAV, and lots of research outputs were produced. A decentralised scheme for spacecraft formation flying via the virtual structure approach is proposed in Refs (5) and (6). As the extension of this study, the authors in Ref. (7) studied the decentralised consensus control of a formation of rigid body spacecraft in the framework of geometric mechanics while accounting for a constant communication time delay between spacecraft. In the field of UAV, the main formation control technologies include model predictive control, bionic algorithm and consistency theory, and the consistency control algorithm based on graph theory gradually becomes the focus of research. Numerical research results are available for Refs (8–12).

Due to the difference in physical structure and motion mechanism, there are huge differences between missiles and UAVs in formation flight control, and the corresponding research results are still lacking. The formation tracking protocols were proposed by using the ideas of proportion and differential controller for the multiple BTT missiles system[13] and multiple aircrafts system[14]. Wei et al.[15] designed an adaptive controller to compensate the coupling effects caused by attitude motion. The dynamic surface controllers were introduced for solving the formation tracking issues for multiple missiles system in Ref. (16). In Ref. (17), cost functions were defined by considering the formation tracking error and control input, and the optimal formation tracking protocol can be obtained by using the functional calculus of variation, where the velocity and flight path angle were defined as the input vector.

Based on the high-precision positioning requirement of multiple flight vehicles for the target in a long distance, this paper mainly focuses on the cooperative control law design of formation configuration. The structure of this paper is organised as follows. In Section 2, the problem statement is provided, and the kinematics models of the flight vehicles are also built. Next the configuration parameters that satisfy the constraints are designed in the Section 3. The control law with considering the effects of the external disturbance and the first-order dynamic characteristic of the autopilot is designed, and a novel improved control method is proposed in the Section 4. Simulation results and analysis are shown in the Section 5. Finally, the concluding remarks are offered in the last section.

2.0 PROBLEM FORMULATION AND MATHEMATICAL MODEL

Considering the following scenario that multiple flight vehicles are scatted by a parent vehicle at a certain height h, and all flight vehicles can be numbered as $i = 1, 2, ..., n$ to easily subsequent descriptions. Obviously, these sub-vehicles would perform inertial flight in the absence of control, so the system configuration cannot be guaranteed to achieve high-precision cooperative detection during the mid-guidance phase. Therefore, it is assumed that if the finite time convergent control strategy is designed to make all sub-vehicles form the expected distances and angles at the preset distance R between the formation system and the target,

https://doi.org/10.1017/aer.2021.30 Published online by Cambridge University Press

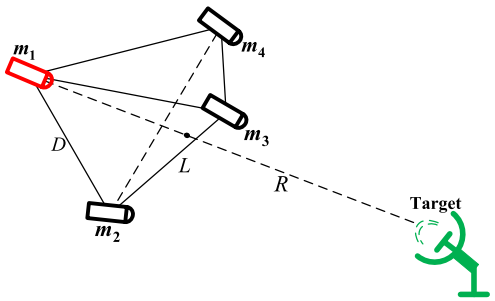

Figure 1. Relative position between system configuration and target.

and then maintain the configuration before the terminal guidance phase. Combine with the characteristics of detection device, the space formation constraints are listed as follows[18,19]:

(1) Configuration constraints. Assume that $n = 4$, and then these four sub-vehicles can be named as m_1, m_2, m_3, m_4. These four sub-vehicles form the tetrahedron structure, as shown in Fig. 1, where the 1^{th} flight vehicle in the back and the other three in the front; The connection line between the 1^{th} one and the target is basically perpendicular to the plane where the other three ones are located in, and the offset angle relative to the centre of the plane cannot over 10%.

(2) Distance constraints between sub-vehicles (m_2, m_3, m_4). Considering the operating distance of the radar detection device, choose$R = 300$km. Besides, to guarantee the positioning accuracy indexes of configuration system, choose $L \geq 6$km; the distances between the 1^{th} flight vehicle m_1 and the other three are not more than 10km, i.e. $D \leq 10$km; the distance between the 1^{th} flight vehicle and the plane formed by the other three sub-vehicles satisfies $1.5 \sim 3.5$km.

For the formation control of multiple flight vehicles, which mainly focus on the motion of the centre of mass. Thus, this paper assumes that the body attitude of each flight vehicle keeps steady during the flight and points to the target when the configuration is formed. The "virtual leader-follower"[20,21] method is used to design the control scheme, that is, a virtual rigid body is used to describe the motion of the whole formation system; however, the four sub-vehicles manoeuver rapidly relative to the virtual leader until meet the configuration constraints. As shown in Fig. 2, define o stands for the virtual leader; $ox_sy_sz_s$is the relative coordinate system of the line-of-sight (LOS), and $\overrightarrow{ox_s}$ points to the target; $\mathbf{T}_i$ is the expected terminal position for the i^{th} sub-vehicle m_i when the configuration is formed. The 1^{th} sub-vehicle m_1 moves backward to T_1 relative to the virtual leader o, and the 2^{th} sub-vehicle m_2 moves downward to T_2, while the 3^{th} one m_3 and the 4^{th} one m_4 move right and left to T_3 and T_4 respectively.

The mathematical model of motion for each flight vehicle in the relative LOS coordinate system can be described as

$$\begin{aligned} \dot{\boldsymbol{x}}_{\boldsymbol{s,i}}(\boldsymbol{t}) &= \boldsymbol{v}_{\boldsymbol{s,i}}(\boldsymbol{t}) \\ \dot{\boldsymbol{v}}_{\boldsymbol{s,i}}(\boldsymbol{t}) &= \boldsymbol{a}_{\boldsymbol{s,i}}(\boldsymbol{t}) + \boldsymbol{d}_{\boldsymbol{s}}(\boldsymbol{t}) \end{aligned} \quad \ldots (1)$$

where $\boldsymbol{x}_{\boldsymbol{s,i}} = [x_{si}, y_{si}, z_{si}]^T$ is the position vector of each sub-vehicle; $\boldsymbol{v}_{\boldsymbol{s,i}} = [v_{sxi}, v_{syi}, v_{szi}]^T$ is the velocity vector, while $\boldsymbol{a}_{\boldsymbol{s,i}} = [a_{sxi}, a_{syi}, a_{szi}]^T$ is the acceleration vector of each sub-vehicle

https://doi.org/10.1017/aer.2021.30 Published online by Cambridge University Press

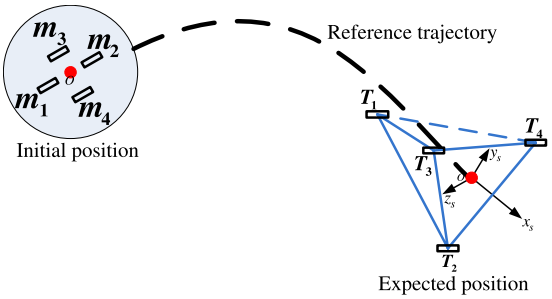

Figure 2. Space manoeuver process of four flight vehicles.

in the LOS frame; $\boldsymbol{d_s}(t)$ is the external disturbance during the flight, and there is $|\boldsymbol{d_s}(t)| \leq \delta$. In addition, define the expected position vector of each sub-vehicle in the LOS coordinate system as $\boldsymbol{x_{q,i}} = [x_{qi}, y_{qi}, z_{qi}]^T$, and the expected velocity vector as $\boldsymbol{v_{q,i}} = [v_{qxi}, v_{qyi}, v_{qzi}]^T$. Considering that the flight task requires these four flight vehicles to maintain the expected formation configuration, thus there exists $v_{qxi} = v_{qyi} = v_{qzi} = 0\text{m/s}$.

3.0 DESIGN OF CONFIGURATION PARAMETERS

According to the configuration constraints described in the Section 2, the expected parameters of each sub-vehicle in the relative LOS coordinate system can be designed. Refer to Fig. 2, assuming that the coordinate vector of virtual leader is $(0, 0, 0)$, and the coordinate vector of the first flight vehicle is $m_1\ (x_1, y_1, z_1)$, while the remain three sub-vehicles are defined as $m_2\ (x_2, y_2, z_2)$, $m_3\ (x_3, y_3, z_3)$, $m_4\ (x_4, y_4, z_4)$, respectively, and the related plane formed by them is defined as $T_2T_3T_4$. The vector connecting the 1^{th} flight vehicle and the target is defined as $\overrightarrow{T_1T}$, and the vector between the virtual leader and the 1^{th} flight vehicle is $\overrightarrow{T_1O}$. Next there exists the following geometric relationship.

(1) The baseline length L_{23}, L_{24}, L_{34} between each sub-vehicle

$$\begin{cases} \Delta x_{32} = x_3 - x_2, \Delta x_{42} = x_4 - x_2, \Delta x_{43} = x_4 - x_3 \\ \Delta y_{32} = y_3 - y_2, \Delta y_{42} = y_4 - y_2, \Delta y_{43} = y_4 - y_3 \\ \Delta z_{32} = z_3 - z_2, \Delta z_{42} = z_4 - z_2, \Delta z_{43} = z_4 - z_3 \end{cases} \quad \ldots (2)$$

$$\begin{cases} L_{23} = \sqrt{(\Delta y_{32})^2 + (\Delta z_{32})^2} \\ L_{24} = \sqrt{(\Delta y_{42})^2 + (\Delta z_{42})^2} \\ L_{34} = \sqrt{(\Delta y_{43})^2 + (\Delta z_{43})^2} \end{cases} \quad \ldots (3)$$

(2) The distance L_0 between the 1^{th} sub-vehicle and the plane $T_2T_3T_4$

$$L_0 = \frac{L_{0f}}{L_{0m}} \quad \ldots (4)$$

https://doi.org/10.1017/aer.2021.30 Published online by Cambridge University Press

Table 1
Expected parameters of each flight vehicle

Number of flight vehicle	Value/m
m_1	$\boldsymbol{T}_1$ $(-2500, 0, 0)$
m_2	$\boldsymbol{T}_2$ $(0, -4042, 0)$
m_3	$\boldsymbol{T}_3$ $(0, 2021, 3500)$
m_4	$\boldsymbol{T}_4$ $(0, 2021, -3500)$

where

$$L_{0f} = |(x_2 - x_1)(\Delta z_{32}\Delta y_{42} - \Delta y_{32}\Delta z_{42}) + (y_2 - y_1)(\Delta x_{32}\Delta z_{42} - \Delta z_{32}\Delta x_{42}) + (z_2 - z_1)(\Delta y_{32}\Delta x_{42} - \Delta x_{32}\Delta y_{42})|,$$

$$L_{0m} = \sqrt{\left((\Delta y_{32}\Delta z_{42} - \Delta z_{32}\Delta y_{42})^2 + (\Delta z_{32}\Delta x_{42} - \Delta x_{32}\Delta z_{42})^2 + (\Delta x_{32}\Delta y_{42} - \Delta y_{32}\Delta x_{42})^2\right)}.$$

(3) The offset angle $\Delta center$ between $\overrightarrow{T_1 T}$ and $\overrightarrow{T_1 O}$

$$\begin{cases} \Delta x = \dfrac{x_2 + x_3 + x_4}{3} - x_1 \\ \Delta y = \dfrac{y_2 + y_3 + y_4}{3} - y_1 \\ \Delta z = \dfrac{z_2 + z_3 + z_4}{3} - z_1 \end{cases} \quad \ldots (5)$$

$$\Delta center = \arccos\left(\frac{\Delta x}{\sqrt{\Delta x^2 + \Delta y^2 + \Delta z^2}}\right) \quad \ldots (6)$$

According to Equations (2)–(6), the expected coordinate vector of each sub-vehicle relative to the virtual leader in the LOS coordinate system can be designed, as shown in Table 1.

Whether these parameters shown in Table 1 meet the formation constraints described in the Section 2 or not, which can be judged by substituting them into Equations (2)–(6) yields

(a) $\Delta center = 0°$, which stands for the 1^{th} flight vehicle is projected on the centre of the plane $T_2T_3T_4$ and thus meet the requirement of offset angle;

(b) $L_{23}, L_{24}, L_{34} = 7$km, which stands for the baseline length between each sub-vehicle is more than 6km;

(c) $L_0 = 2.5$km, which means that the distance of the 1^{th} flight vehicle relative to the plane $T_2T_3T_4$ is between 1.5 and 3.5km.

In summary, the position parameters of each flight vehicle shown in Table 1 meet the configuration constraints described in the Section 2. Then the appropriate control law is designed in the Section 4 to control the four flight vehicles to fly to their expected positions and simulation verification is performed in the Section 5.

https://doi.org/10.1017/aer.2021.30 Published online by Cambridge University Press

4.0 DESIGN OF CONTROL LAW

In this section, the control law is completely designed in the following three steps. The first is to design the NTSMC law with considering the external disturbances of the system; the second is design the second-order NTSMC law with considering the dynamic characteristic of the autopilot of flight vehicle; the third one is that a novel improved control law is proposed to guarantee the finite time convergence of the system errors, and also effectively suppress the small chattering phenomenon of the sliding mode surfaces and the acceleration responses.

4.1 Design of NTSMC law

For system (1), define the flight error vector and velocity error vector of each sub-vehicle in the LOS coordinate system as

$$\begin{aligned} \boldsymbol{e}_{1,i} &= \boldsymbol{x}_{s,i} - \boldsymbol{x}_{q,i} \\ \boldsymbol{e}_{2,i} &= \boldsymbol{v}_{s,i} \end{aligned} \quad \ldots (7)$$

Differentiating Equation (7) with respect to time can be obtained as

$$\begin{aligned} \dot{\boldsymbol{e}}_{1,i} &= \boldsymbol{e}_{2,i} \\ \dot{\boldsymbol{e}}_{2,i} &= \boldsymbol{a}_{s,i}(\boldsymbol{t}) + \boldsymbol{d}_s(\boldsymbol{t}) \end{aligned} \quad \ldots (8)$$

For system (8), take any sub-vehicle as an example, and choose the NTSM as

$$\boldsymbol{s} = \boldsymbol{e}_1 + \beta sig^{\gamma}(\boldsymbol{e}_2) \quad \ldots (9)$$

where $\beta > 0, 1 < \gamma < 2, sig^{\gamma}(\boldsymbol{e}_2) = |\boldsymbol{e}_2|^{\gamma} \operatorname{sgn}(\boldsymbol{e}_2)$, is the sign function.

Differentiating Equation (9) with respect to time yields

$$\begin{aligned} \dot{\boldsymbol{s}} &= \dot{\boldsymbol{e}}_1 + \beta\gamma |\boldsymbol{e}_2|^{\gamma-1} \dot{\boldsymbol{e}}_2 \\ &= \boldsymbol{e}_2 + \beta\gamma |\boldsymbol{e}_2|^{\gamma-1} (\boldsymbol{a}_s + \boldsymbol{d}_s(\boldsymbol{t})) \end{aligned} \quad \ldots (10)$$

Choose the fast terminal sliding mode reaching law as

$$\dot{\boldsymbol{s}} = -k_1 \boldsymbol{s} - k_2 sig^{\rho}(\boldsymbol{s}) \quad \ldots (11)$$

where $k_1 > 0, k_2 > 0, 0 < \rho < 1$. Compare Equations (10) and (11), the adaptive NTSMC law can be obtained as

$$\boldsymbol{a}_s = -\frac{sig^{2-\gamma}(\boldsymbol{e}_2)}{\beta\gamma} - k_1 \boldsymbol{s} - k_2 sig^{\rho}(\boldsymbol{s}) - \varepsilon \operatorname{sgn}(\boldsymbol{s}) \quad \ldots (12)$$

where $\varepsilon \operatorname{sgn}(\boldsymbol{s})$ is used to compensate the external disturbance. if ε is too large, the control variable $\boldsymbol{a}_s$ will be too large; However, if ε is too small, it will easily cause system instability. Define $\tilde{\delta} = \delta - \hat{\delta}$, in which $\hat{\delta}$ is the estimated value of the variable δ. Assume that there exists $\left|\tilde{\delta}\right| < \varepsilon_1$ for any kinds of disturbance, and ε_1 is a small normal number. Then the adaptive gain ε in Equation (12) can be designed as

$$\varepsilon = \hat{\delta} + \varepsilon_1, \dot{\hat{\delta}} = \lambda\beta\gamma |\boldsymbol{e}_2|^{\gamma-1} |\boldsymbol{s}| \quad \ldots (13)$$

where $\lambda > 0$ is the weighting coefficient to be designed.

https://doi.org/10.1017/aer.2021.30 Published online by Cambridge University Press

For system (8) and sliding mode (9), the control law (12) can guarantee that the formation system controlling errors converges to zero in a finite time.

Proof of Theorem 1: Substituting Equation (12) into Equation (10) yields

$$\dot{\boldsymbol{s}} = \beta\gamma|\boldsymbol{e_2}|^{\gamma-1}\left(-k_1\boldsymbol{s} - k_2 sig^{\rho}(\boldsymbol{s})\right) + \boldsymbol{d_s}(\boldsymbol{t}) - \varepsilon \mathrm{sgn}(\boldsymbol{s}) \quad \ldots(14)$$

Define the following Lyapunov function

$$\boldsymbol{V} = \frac{1}{2}\boldsymbol{s}^2 + \frac{1}{2\lambda}\tilde{\delta}^2 \quad \ldots(15)$$

Differentiating Equation (15) with respect to time yields

$$\begin{aligned}\dot{\boldsymbol{V}} &= \boldsymbol{s}\dot{\boldsymbol{s}} + \frac{1}{\lambda}\tilde{\delta}\dot{\tilde{\delta}} \\ &= \beta\gamma|\boldsymbol{e_2}|^{\gamma-1}\boldsymbol{s}\left(-k_1\boldsymbol{s} - k_2 sig^{\rho}(\boldsymbol{s}) + \boldsymbol{d_s}(\boldsymbol{t}) - \varepsilon\mathrm{sgn}(\boldsymbol{s})\right) + \frac{1}{\lambda}\tilde{\delta}\left(\dot{\tilde{\delta}} - \dot{\hat{\delta}}\right) \\ &\le \beta\gamma|\boldsymbol{e_2}|^{\gamma-1}\left(-k_1\boldsymbol{s}^2 - k_2|\boldsymbol{s}|^{\rho+1} + \delta|\boldsymbol{s}| - \varepsilon_1|\boldsymbol{s}| - \hat{\delta}|\boldsymbol{s}|\right) - \frac{1}{\lambda}\tilde{\delta}\dot{\hat{\delta}} \end{aligned} \quad \ldots(16)$$

Substituting Equation (13) into Equation (16) yields

$$\begin{aligned}\dot{\boldsymbol{V}} &\le \beta\gamma|\boldsymbol{e_2}|^{\gamma-1}\left(-k_1\boldsymbol{s}^2 - k_2|\boldsymbol{s}|^{\rho+1} + \delta|\boldsymbol{s}| - \varepsilon_1|\boldsymbol{s}| - \hat{\delta}|\boldsymbol{s}|\right) - \tilde{\delta}\beta\gamma|\boldsymbol{e_2}|^{\gamma-1}|\boldsymbol{s}| \\ &\le \beta\gamma|\boldsymbol{e_2}|^{\gamma-1}\left(-k_1\boldsymbol{s}^2 - k_2|\boldsymbol{s}|^{\rho+1} - \varepsilon_1|\boldsymbol{s}|\right) \\ &\le 0 \end{aligned} \quad \ldots(17)$$

Lemma 1 (22). Consider the nonlinear system $\dot{x} = f(x,t), x \in R^n$, and if there exists a positive defined Lyapunov function $V(x)$and the parameters $\beta_1 > 0, \beta_3 > 0$ and $\beta_2 \in (0,1)$ satisfy

$$\dot{V}(t) + \beta_3 V(t) + \beta_1 V^{\beta_2}(t) \le 0 \quad \ldots(18)$$

Then the system state can reach zero in a finite time T_{reach}, which is given by

$$T_{reach} \le \frac{1}{\beta_3(1-\beta_2)} \ln \frac{\beta_3 V^{1-\beta_2}(t_0) + \beta_1}{\beta_1} \quad \ldots(19)$$

where $V(x_0)$ is the initial value of $V(x)$.

According to Lemma 1, since ε_1 is a small normal number, the system (8) can converge to the sliding mode surface; When $\boldsymbol{e_2} = 0$ and $\boldsymbol{s} \neq 0$, the sliding mode surface (9) shows that $\boldsymbol{e_1} \neq 0$, which means that the system do not reach the stable state, and thus $\dot{\boldsymbol{V}}$ is not equal to zero, that is, $\dot{\boldsymbol{V}} < 0$ at the current time. From Equations (16) and (17), it is obvious that the system will converge to zero in a finite time in this case; when the sliding mode surface $\boldsymbol{s} = 0$, it indicates that the system state vectors $\boldsymbol{e_1}$ and $\boldsymbol{e_2}$ reach the equilibrium point, that is, each sub-vehicle flies to the desired terminal position, and the velocity relative to the virtual leader is 0m/s.

Here the Proof of Theorem 1 is completed.

https://doi.org/10.1017/aer.2021.30 Published online by Cambridge University Press

4.2 Design of control law considering the dynamic characteristic of autopilot

Based on Section 4.1, further considering the first-order dynamic characteristic of the autopilot, and then the adaptive second-order sliding mode control (SOSMC) law with finite time convergence is designed. The first-order dynamic characteristic of the autopilot can be expressed as

$$\dot{\boldsymbol{a}}_{m,i} = -\frac{1}{\tau}\boldsymbol{a}_{m,i} + \frac{1}{\tau}\boldsymbol{u}_i \quad \ldots(20)$$

where τ is the delay time constant of autopilot; $\boldsymbol{u}_i = \boldsymbol{a}_{s,i}$ is acceleration command vector; $\boldsymbol{a}_{m,i}$ is the acceleration vector in the LOS coordinate system.

Combine with Equation (20), the system (8) can be further rewritten as

$$\begin{aligned}
\dot{\boldsymbol{e}}_{1,i} &= \boldsymbol{e}_{2,i} \\
\dot{\boldsymbol{e}}_{2,i} &= \boldsymbol{e}_{3,i} \\
\dot{\boldsymbol{e}}_{3,i} &= -\frac{1}{\tau}\boldsymbol{a}_{m,i} + \frac{1}{\tau}\boldsymbol{u}_i + \boldsymbol{d}_s(\boldsymbol{t})
\end{aligned} \quad \ldots(21)$$

For Equation (21), choose the linear sliding mode surface as

$$\boldsymbol{s}_1 = k_0\boldsymbol{e}_1 + \boldsymbol{e}_2 \quad \ldots(22)$$

where $k_0 > 0$ is the control parameter to be designed.

Differentiating Equation (22) with respect to time once and twice respectively yields

$$\begin{aligned}
\dot{\boldsymbol{s}}_1 &= k_0\dot{\boldsymbol{e}}_1 + \dot{\boldsymbol{e}}_2 \\
&= k_0\boldsymbol{e}_2 + \boldsymbol{e}_3
\end{aligned} \quad \ldots(23)$$

$$\begin{aligned}
\ddot{\boldsymbol{s}}_1 &= k_0\dot{\boldsymbol{e}}_2 + \dot{\boldsymbol{e}}_3 \\
&= k_0\boldsymbol{e}_3 + \dot{\boldsymbol{e}}_3 \\
&= k_0\boldsymbol{e}_3 - \frac{1}{\tau}\boldsymbol{a}_{m,i} + \frac{1}{\tau}\boldsymbol{u}_i + \boldsymbol{d}_s(\boldsymbol{t})
\end{aligned} \quad \ldots(24)$$

To assure that the flight state errors of these four flight vehicles converge quickly in a finite time, then take $\boldsymbol{s}_1$ and $\dot{\boldsymbol{s}}_1$ as state variables, and choose the following non-singular terminal sliding mode as

$$\boldsymbol{s}_2 = \boldsymbol{s}_1 + \beta sig^{\gamma}(\dot{\boldsymbol{s}}_1) \quad \ldots(25)$$

where $sig^{\gamma}(\dot{\boldsymbol{s}}_1) = |\dot{\boldsymbol{s}}_1|^{\gamma}\operatorname{sgn}(\dot{\boldsymbol{s}}_1)$, and the other parameters are consistent with Equation (9). Differentiating Equation (25) yields

$$\begin{aligned}
\dot{\boldsymbol{s}}_2 &= \dot{\boldsymbol{s}}_1 + \beta\gamma|\dot{\boldsymbol{s}}_1|^{\gamma-1}\ddot{\boldsymbol{s}}_1 \\
&= \dot{\boldsymbol{s}}_1 + \beta\gamma|\dot{\boldsymbol{s}}_1|^{\gamma-1}\left(k_0\boldsymbol{e}_3 - \frac{1}{\tau}\boldsymbol{a}_{m,i} + \frac{1}{\tau}\boldsymbol{u}_i + \boldsymbol{d}_s(\boldsymbol{t})\right)
\end{aligned} \quad \ldots(26)$$

Similarly, in this case, the control law can be obtained as

$$\boldsymbol{u}_i = -\frac{\tau}{\beta\gamma}|\dot{\boldsymbol{s}}_1|^{2-\gamma}\operatorname{sgn}(\dot{\boldsymbol{s}}_1) - \frac{\tau}{\beta\gamma}|\dot{\boldsymbol{s}}_1|^{1-\gamma}\left[k_1\boldsymbol{s}_2 + k_2 sig^{\rho}(\boldsymbol{s}_2)\right] - (\tau k_0 - 1)\boldsymbol{e}_3 - \tau\boldsymbol{d}_s(\boldsymbol{t}) \quad \ldots(27)$$

https://doi.org/10.1017/aer.2021.30 Published online by Cambridge University Press

To avoid $\frac{\tau}{\beta\gamma}|\dot{\boldsymbol{s}}_{\mathbf{1}}|^{1-\gamma}$ occurs singularity when $\dot{\boldsymbol{s}}_{\mathbf{1}} \to 0$, Equation (27) can be simplified as

$$\boldsymbol{u_i} = -\frac{\tau}{\beta\gamma}|\dot{\boldsymbol{s}}_{\mathbf{1}}|^{2-\gamma}\operatorname{sgn}(\dot{\boldsymbol{s}}_{\mathbf{1}}) - \tau\left[k_1\boldsymbol{s_2} + k_2 sig^{\rho}(\boldsymbol{s_2})\right] - (\tau k_0 - 1)\,\boldsymbol{e}_3 - \tau\boldsymbol{d_s}(\boldsymbol{t}) \quad \ldots(28)$$

Therefore, according to Equation (28), the adaptive NTSMC law with considering the first-order dynamic characteristic of the autopilot can be written as

$$\boldsymbol{u_i} = -\frac{\tau}{\beta\gamma}|\dot{\boldsymbol{s}}_{\mathbf{1}}|^{2-\gamma}\operatorname{sgn}(\dot{\boldsymbol{s}}_{\mathbf{1}}) - \tau\left[k_1\boldsymbol{s_2} + k_2 sig^{\rho}(\boldsymbol{s_2})\right] - (\tau k_0 - 1)\,\boldsymbol{e}_3 - \tau\varepsilon\operatorname{sgn}(\boldsymbol{s_2}) \quad \ldots(29)$$

where the adaptive gain ε in Equation (29) can be taken as

$$\varepsilon = \hat{\delta} + \varepsilon_1, \dot{\hat{\delta}} = \tau\lambda\beta\gamma|\boldsymbol{e_2}|^{\gamma-1}|\boldsymbol{s_2}| \quad \ldots(30)$$

The proof and related discussion of stability is similar to the Section 4.1.

4.3 A novel control law

In Section 4.2, the second-order sliding control law is designed, which ensure that the formation configuration of the system converges in a finite time; however, this control algorithm will result in the small-amplitude chattering phenomenon of the sliding mode surfaces and control variables at the equilibrium point. Hence, in this section, a novel improved control law is proposed, which makes the sliding mode surfaces asymptotically converge to zero without crossing the zero point. Meanwhile, the chattering of acceleration responses is effectively eliminated, and the robustness of the system is subsequently enhanced.

Define the sliding mode function of any sub-vehicle as

$$\boldsymbol{s}_1 = \boldsymbol{y}(\boldsymbol{x}) = 0 \quad \ldots(31)$$

For Equation (31), the first-order differential equation and second-order differential equation can be expressed as

$$\dot{\boldsymbol{s}}_1 = \mathbf{h}(\boldsymbol{x}) \quad \ldots(32)$$

$$\ddot{\boldsymbol{s}}_1 = \boldsymbol{f}(\boldsymbol{x}) + \boldsymbol{b}(\boldsymbol{x})\,\boldsymbol{u} \quad \ldots(33)$$

For Equations (32) and (33), in which $\boldsymbol{h}(\boldsymbol{x}), \boldsymbol{f}(\boldsymbol{x}), \boldsymbol{b}(\boldsymbol{x})$are the known functions relating to the system.

For the sliding function (31) and the first-order differential equation (32), which need to converge to zero at the given time t_r, and define the following Lyapunov function as

$$\boldsymbol{V}_1 = \frac{1}{2}\boldsymbol{s}_1{}^2 \quad \ldots(34)$$

Differentiating Equation (34) with respect to time yields

$$\dot{\boldsymbol{V}}_1 = \boldsymbol{s}_1\dot{\boldsymbol{s}}_1 \quad \ldots(35)$$

https://doi.org/10.1017/aer.2021.30 Published online by Cambridge University Press

To assure that the sliding mode surface (31) converges to zero in a finite time, that is $\dot{\boldsymbol{V}}_{\mathbf{1}} \leq 0$, and thus design $\dot{\boldsymbol{s}}_1$ as

$$\dot{\boldsymbol{s}}_1 = -\frac{\mathrm{n}\boldsymbol{s}_1}{\mathrm{t}_r - \mathrm{t}}, \mathrm{n} > 1 \quad \ldots (36)$$

where $\mathrm{n} > 1$ is the coefficient to be designed. Substituting Equation (36) into Equation (35) yields

$$\dot{\boldsymbol{V}}_1 = -\frac{\mathrm{n}\boldsymbol{s}_1{}^2}{\mathrm{t}_r - \mathrm{t}} \quad \ldots (37)$$

Substituting Equation (34) into Equation (37) yields

$$\dot{\boldsymbol{V}}_1 = -\frac{2\mathrm{n}\boldsymbol{V}_1}{\mathrm{t}_r - \mathrm{t}} \quad \ldots (38)$$

Integrating Equation (38) yields

$$\int_{t_0}^{t} \dot{\boldsymbol{V}}_{\mathbf{1}}(t)\, dt = \boldsymbol{V}_{\mathbf{1}}(t) = \frac{\boldsymbol{V}_{\mathbf{1}}(t_0)}{(t_r - t_0)^{2n}}(t_r - t)^{2n} \quad \ldots (39)$$

where $\lim_{t \to t_r} (t_r - t)^{2n}$ is equal to zero when $n > 0.5$, and thus the Lyapunov function $\boldsymbol{V}_{\mathbf{1}}(t)$ can converge to zero within the desired time t_r and the sliding mode surface $\boldsymbol{s}_1$ can also reach zero at the same time(23). For the first-order derivative $\dot{\boldsymbol{s}}_1$ of the sliding mode surface, it can converge to zero within the designed time t_r only when $n > 1$. Due to the initial value of $\dot{\boldsymbol{s}}_1$ totally depend on the initial conditions of the problem, thus $\dot{\boldsymbol{s}}_1$ may not meet the expected trajectory given by Equation (36) at the initial stage. Therefore, the control command needs to be able to make $\dot{\boldsymbol{s}}_1$ reach the trajectory shown in Equation (36) within a limited time. Under this circumstance, define a new sliding mode surface as

$$\boldsymbol{s}_2 = \dot{\boldsymbol{s}}_1 + \frac{\mathrm{n}\boldsymbol{s}_1}{\mathrm{t}_r - \mathrm{t}} \quad \ldots (40)$$

Differentiating Equation (40) with respect to time yields

$$\begin{aligned} \dot{\boldsymbol{s}}_2 &= \ddot{\boldsymbol{s}}_1 + \frac{\mathrm{n}\dot{\boldsymbol{s}}_1(\mathrm{t}_r - \mathrm{t}) + \mathrm{n}\boldsymbol{s}_1}{(\mathrm{t}_r - \mathrm{t})^2} \\ &= \boldsymbol{f}(\boldsymbol{x}) + \frac{\mathrm{n}\dot{\boldsymbol{s}}_1(\mathrm{t}_r - \mathrm{t}) + \mathrm{n}\boldsymbol{s}_1}{(\mathrm{t}_r - \mathrm{t})^2} + \boldsymbol{b}(\boldsymbol{x})\boldsymbol{u} \end{aligned} \quad \ldots (41)$$

Define the following Lyapunov function as

$$\boldsymbol{V}_2 = \frac{1}{2}\boldsymbol{s}_2{}^2 \quad \ldots (42)$$

Differentiating Equation (42) with respect to time yields

$$\dot{\boldsymbol{V}}_2 = \boldsymbol{s}_2\dot{\boldsymbol{s}}_2 = \boldsymbol{s}_2\left[\boldsymbol{f}(\boldsymbol{x}) + \frac{\mathrm{n}\dot{\boldsymbol{s}}_1(\mathrm{t}_r - t) + \mathrm{n}\boldsymbol{s}_1}{(\mathrm{t}_r - \mathrm{t})^2} + \boldsymbol{b}(\boldsymbol{x})\boldsymbol{u}\right] \quad \ldots (43)$$

https://doi.org/10.1017/aer.2021.30 Published online by Cambridge University Press

To guarantee that V_2 converges to zero in a finite time, and then the control command can be designed as

$$\boldsymbol{u} = -\frac{1}{\boldsymbol{b}(\boldsymbol{x})}\left(\boldsymbol{f}(\boldsymbol{x}) + \frac{\mathrm{n}\dot{\boldsymbol{s}}_1(\mathrm{t}_r - \mathrm{t}) + \mathrm{n}\boldsymbol{s}_1}{(\mathrm{t}_r - \mathrm{t})^2} + \eta\mathrm{sgn}\left(\dot{\boldsymbol{s}}_1 + \frac{\mathrm{n}\boldsymbol{s}_1}{\mathrm{t}_r - \mathrm{t}}\right)\right) \quad \ldots(44)$$

where $\eta > 0$ is the control coefficient to be designed, which can affect the convergence speed of the system; substituting Equation (44) into Equation (43) yields

$$\dot{V}_2 < -\eta|\boldsymbol{s}_2| \le 0, \qquad \eta > 0 \quad \ldots(45)$$

The above derivation can be summarised as Theorem 2.

Theorem 2. Assume that there is a second-order sliding mode surface $\boldsymbol{s}_1$, and its first-order derivative and second-order derivative can be expressed as $\dot{\boldsymbol{s}}_1 = -\mathrm{n}\boldsymbol{s}_1/(\mathrm{t}_r - \mathrm{t})$, $\mathrm{n} > 1$ and $\ddot{\boldsymbol{s}}_1 = \boldsymbol{f}(\boldsymbol{x}) + \boldsymbol{b}(\boldsymbol{x})\boldsymbol{u}$ respectively. Define another sliding mode surface $\boldsymbol{s}_2 = \dot{\boldsymbol{s}}_1 + \mathrm{n}\boldsymbol{s}_1/(\mathrm{t}_r - \mathrm{t})$, and its related derivative is $\dot{\boldsymbol{s}}_2 = \ddot{\boldsymbol{s}}_1 + [\mathrm{n}\dot{\boldsymbol{s}}_1(\mathrm{t}_r - \mathrm{t}) + \mathrm{n}\boldsymbol{s}_1]/(\mathrm{t}_r - \mathrm{t})^2$. In this case, $\boldsymbol{s}_1$ and $\dot{\boldsymbol{s}}_1$ both can converge to zero in a finite time, and the system to be controlled can reach the steady state within the designed time t_r by using the control law shown in Equation (44).

For system (21), choose the sliding mode surface (22) and its corresponding first-order derivative and second-order derivative are still shown as Equations (23) and (24). According to Equation (41), there exists

$$\begin{aligned}\dot{\boldsymbol{s}}_2 &= \ddot{\boldsymbol{s}}_1 + \frac{\mathrm{n}\dot{\boldsymbol{s}}_1(\mathrm{t}_r - \mathrm{t}) + \mathrm{n}\boldsymbol{s}_1}{(\mathrm{t}_r - \mathrm{t})^2} \\ &= \mathrm{k}_0\boldsymbol{e}_3 + \dot{\boldsymbol{e}}_3 + \frac{\mathrm{n}\dot{\boldsymbol{s}}_1(\mathrm{t}_r - \mathrm{t}) + \mathrm{n}\boldsymbol{s}_1}{(\mathrm{t}_r - \mathrm{t})^2} \\ &= \mathrm{k}_0\boldsymbol{e}_3 + \left(-\frac{1}{\tau}\boldsymbol{a}_m + \boldsymbol{d}_s(\boldsymbol{t})\right) + \frac{1}{\tau}\boldsymbol{u} + \frac{\mathrm{n}\dot{\boldsymbol{s}}_1(\mathrm{t}_r - \mathrm{t}) + \mathrm{n}\boldsymbol{s}_1}{(\mathrm{t}_r - \mathrm{t})^2}\end{aligned} \quad \ldots(46)$$

Based on Theorem 2, for the sliding mode surface $\boldsymbol{s}_1$ and $\boldsymbol{s}_2$, the control law can be designed as

$$\boldsymbol{u} = -\tau\left(\mathrm{k}_0\boldsymbol{e}_3 + \left(-\frac{1}{\tau}\boldsymbol{a}_m + \boldsymbol{d}_s(\boldsymbol{t})\right) + \frac{\mathrm{n}\dot{\boldsymbol{s}}_1(\mathrm{t}_r - \mathrm{t}) + \mathrm{n}\boldsymbol{s}_1}{(\mathrm{t}_r - \mathrm{t})^2} + \eta\mathrm{sgn}\left(\dot{\boldsymbol{s}}_1 + \frac{\mathrm{n}\boldsymbol{s}_1}{\mathrm{t}_r - \mathrm{t}}\right)\right) \quad \ldots(47)$$

The control law (47) can make the system state errors converge to zero within a finite time t_r, that is, the system meets the expected space formation configuration constraints listed in the Section 2. In Equation (47), $\boldsymbol{d}_s(\boldsymbol{t})$ is the disturbance vector, and it is assumed that the second-order derivative meets $|\ddot{\boldsymbol{d}}_s(\boldsymbol{t})| < \delta$. For the differential equation $\dot{\boldsymbol{e}}_{3,i} = -\frac{1}{\tau}\boldsymbol{a}_{m,i} + \frac{1}{\tau}\boldsymbol{u}_i + \boldsymbol{d}_s(\boldsymbol{t})$ shown in the system (21), the following sliding mode disturbance observer can be designed as[24]

$$\begin{aligned}\dot{\boldsymbol{z}}_0 &= \boldsymbol{v}_0 - \frac{1}{\tau}\boldsymbol{a}_m + \frac{1}{\tau}\boldsymbol{u}, \\ \boldsymbol{v}_0 &= -\lambda_2\delta^{1/3}|\boldsymbol{z}_0 - \boldsymbol{e}_3|^{2/3}\mathrm{sgn}|\boldsymbol{z}_0 - \boldsymbol{e}_3| + \boldsymbol{z}_1\end{aligned}$$

https://doi.org/10.1017/aer.2021.30 Published online by Cambridge University Press

$$\dot{\boldsymbol{z}}_1 = \boldsymbol{v}_1, \boldsymbol{v}_1 = -\lambda_1 \delta^{1/2} |\boldsymbol{z}_1 - \boldsymbol{v}_0|^{1/2} \text{sgn} |\boldsymbol{z}_1 - \boldsymbol{v}_0| + \boldsymbol{z}_2$$
$$\dot{\boldsymbol{z}}_2 = -\lambda_0 \delta \text{sgn} |\boldsymbol{z}_2 - \boldsymbol{v}_1| \quad \ldots (48)$$

where $\lambda_0 > 0, \lambda_1 > 0, \lambda_2 > 0$ are the observer gains to be designed; $\boldsymbol{z}_1$ is the estimation of $\boldsymbol{d}_s(\boldsymbol{t})$.

5.0 SIMULATION AND ANALYSIS

In this section, for the formation configuration controlling question proposed in the Section 2, the expected space configuration and position parameters of each sub-vehicle are designed in the Section 3. By using the control algorithm deduced in the Section 4, numerical simulations are conducted by using Microsoft Visual Studio 2015 to demonstrate the effectiveness of the proposed control law in the following three cases. The case one (Case 1) is the NTSMC law without considering the dynamic characteristic of autopilot, as shown in Equation (12); the case two (Case 2) is the adaptive SOSMC law with considering the dynamic characteristic of autopilot, as shown in Equation (29); the case three (Case 3) is the novel second-order sliding control law shown in Equation (44), which ensure that the formation configuration of the system converges simultaneously with a designed time and eliminate the chattering phenomenon of the sliding mode surfaces and control commands.

The expected position parameters of each sub-vehicle relative to the virtual leader in the LOS coordinate system are shown in Table 1. The initial simulation parameters are also listed in Table 2, where it is assumed that these four sub-vehicles are scattered when $t = 96.032$s.

It is assumed that the system is affected by the external disturbance shown in Equation (49) during the flight, and the estimation is used to compensate the control law (47).

$$a_{Tx} = 10 \sin(0.5t) \text{ m}/s^2$$
$$a_{Ty} = -5 \sin(0.5t) \text{ m}/s^2$$
$$a_{Tz} = 5 \sin(0.5t) \text{ m}/s^2 \quad \ldots (49)$$

5.1 Simulation results of Case 1

The control parameters in Equations (12) and (13) are designed as follows:$\beta = 0.2, \gamma = 1.2, k_1 = 0.0002, k_2 = 0.5, \rho = 0.9, \lambda = 0.001, \varepsilon_1 = 0.1$. In the simulation, choose the initial parameters of the virtual leader are consistent with the 1^{th} sub-vehicle, and its inertial trajectory is used as the reference trajectory of the formation system. In addition, assume that the maximum available acceleration of each sub-vehicle is 10g, and then the trajectory curves of the virtual leader and each sub-vehicle are given in Fig. 3.

From Fig. 3, it can be seen that the flight height of each sub-vehicle is similar to the form of parabolic trajectory, and all flight vehicles around the virtual leader both fly to their expected positions. When the relative distance R between the virtual leader and the target is equal to 300km, the terminal heights of these four flight vehicles are compared as follows: $m_4 > m_3 > m_1 > m_2$. For lateral trajectory, the manoeuvering distances of the 1^{th} sub-vehicle relative to the virtual leader and the 2^{th} one are relatively small, while the baseline distance between the 3^{th} sub-vehicle and the 4^{th} one is pulled apart, which indicates that the entire formation configuration evolves into a tetrahedron structure with respect to the flight time.

The configuration parameters changing curves with respect to the flight time are shown in Fig. 4. The relative distance L_0 between the 1^{th} sub-vehicle and the plane $T_2T_3T_4$ is shown in

https://doi.org/10.1017/aer.2021.30 Published online by Cambridge University Press

Table 2
Initial parameters of each flight vehicle

Term	Parameter	Value
Initial time	t/s	96.032
Height	h/m	75,000
Initial position for m_1	x_1/m	130,623.467
	y_1/m	73,679.436
	z_1/m	632.494
Initial position for m_2	x_2/m	130,624.467
	y_2/m	73,680.436
	z_2/m	632.494
Initial position for m_3	x_3/m	130,625.467
	y_3/m	73,677.436
	z_3/m	633.494
Initial position for m_4	x_4/m	13,0621.467
	y_4/m	73,677.436
	z_4/m	633.494
Initial velocity	v_x/ (m/s)	2,547.438
	v_y/ (m/s)	997.502
	v_z/ (m/s)	19.242

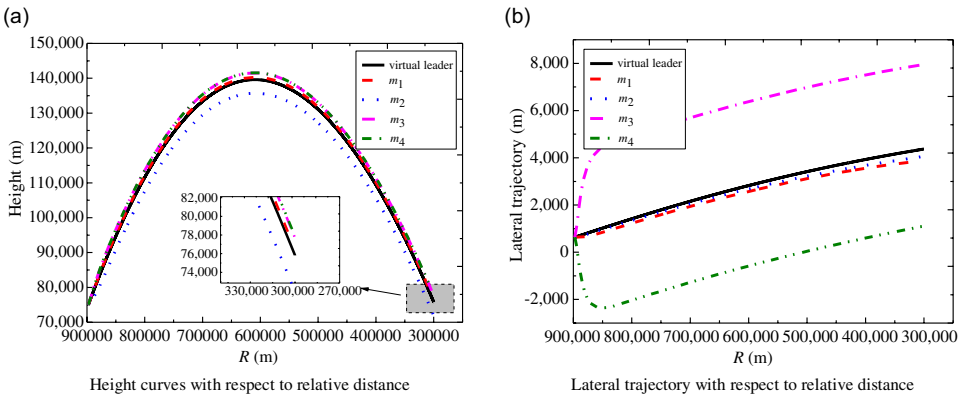

Figure 3. Height and lateral trajectory of flight vehicle.

Fig. 4(a), and it converges to 2.5km when the flight time is equal to 127s, which means that meet the constraint of $1.5 \sim 3.5$km. Figure 4(b) shows the changing curves of baseline lengths L_{23}, L_{24}, L_{34} with respect to the flight time, and they both reach 7kmsimultaneously and thus greater than 6km. In Fig. 4(c), the offset angle of the 1^{th} sub-vehicle with respect to the flight time is given, which finally converges to near 0°.

The sliding mode curves of three-channels with respect to the flight time for each sub-vehicle are shown in Fig. 5. From Fig. 5(a)–(d), it can be seen that the sliding mode surfaces (see Equation (9)) of three-channels for each sub-vehicle both reach a small neighbor of zero with small oscillation in a finite time, and the convergence time is about 118.75s.

To better illustrate the effectiveness of proposed control law, the acceleration commands in the LOS coordinate system can be transferred into the inertial coordinate system, just as

https://doi.org/10.1017/aer.2021.30 Published online by Cambridge University Press

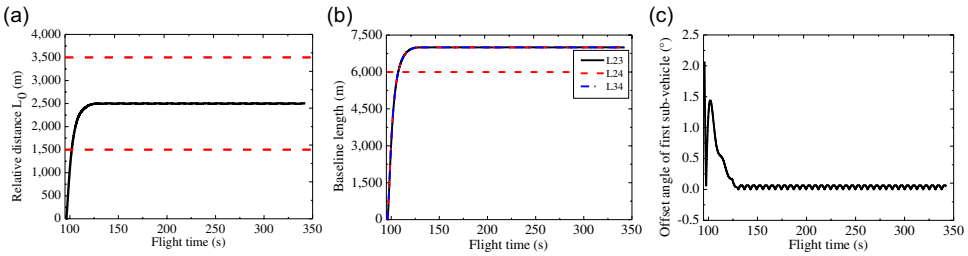

Relative distance L_0 with respect to time

Baseline length L_{23}, L_{24}, L_{34} with respect to time

Offset angle $\Delta\, center$ with respect to time

Figure 4. Configuration parameter curves with respect to time.

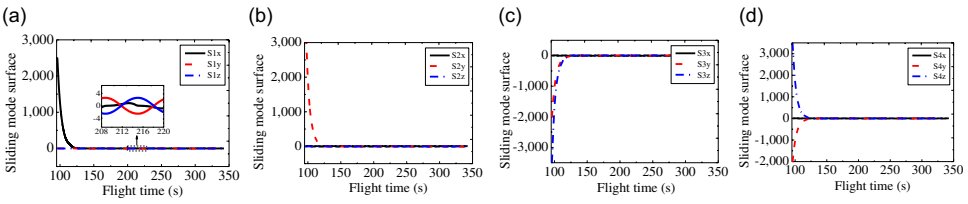

The first sub-vehicle m_1 The second sub-vehicle m_2 The third sub-vehicle m_3 The forth sub-vehicle m_4

Figure 5. Sliding mode curves of three-channels with respect to time.

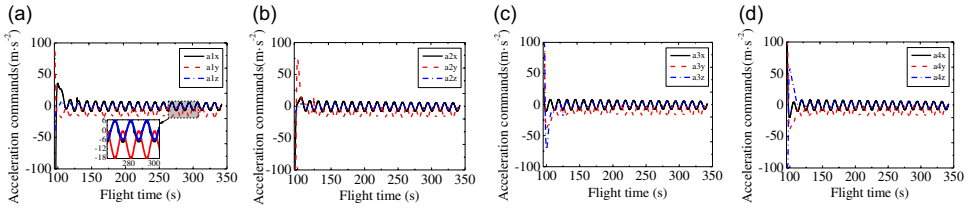

The first sub-vehicle m_1 The second sub-vehicle m_2 The third sub-vehicle m_3 The forth sub-vehicle m_4

Figure 6. Acceleration command curves of three-channels with respect to time.

shown in Fig. 6. From Fig. 6(a)–(d), it can be seen that the acceleration commands of three-channels firstly occur a sharply jump, and then keep a small amplitude of periodic oscillation patter relative to zero which aims to counteract the effects of the external disturbance and gravitational acceleration of projectile body.

It can be observed from Fig. 3, 4, 5 and 6 that the control law shown in Equation (12) can guarantee the rapid generation of the expected formation configuration and ensure that all sub-vehicles simultaneously fly to the preset terminal position, which lays the foundation for the realisation of high precision collaborative detection of the target.

5.2 Simulation results of Case 2

In this section, the initial parameters of each sub-vehicle are listed in Table 2. Considering the dynamic lag time constant of the autopilot $\tau = 0.5$ for Equation (20), and the control parameter $k_0 = 0.03$, while the other control parameters are the same as in Case 1.

https://doi.org/10.1017/aer.2021.30 Published online by Cambridge University Press

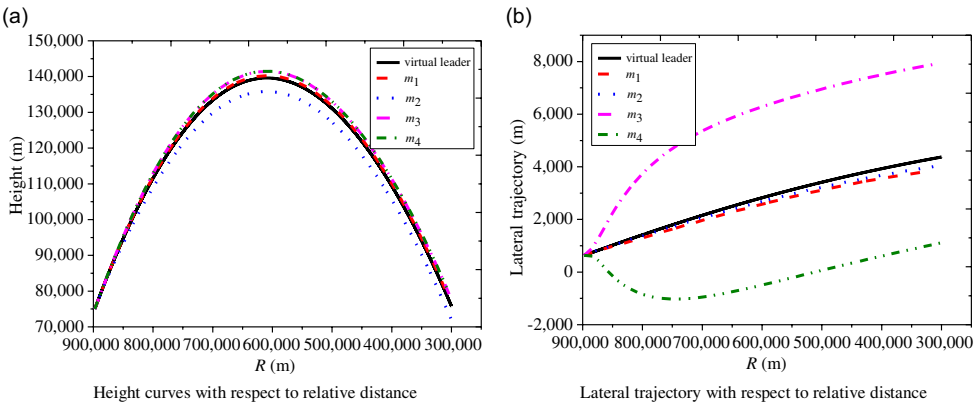

Figure 7. Height and lateral trajectory of flight vehicle.

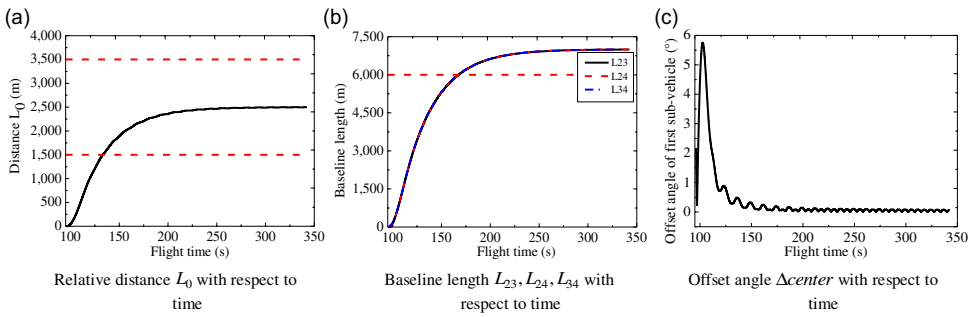

Figure 8. Configuration parameter curves with respect to time.

In this case, the trajectory curves of the virtual leader and each sub-vehicle are given in Fig. 7. From Fig. 7(a), the changing trend of the height curves for each sub-vehicle is consistent with the Case 1; however, for the lateral trajectory curves shown in Fig. 7(b), it can be obviously seen that the convergence time is longer compared with the Case 1.

In this case, the configuration parameters changing curves with respect to the flight time are shown in Fig. 8. From Fig. 8(a)–(c), it can be seen that four sub-vehicles both reach the expected positions, and the convergence time of the formation configuration is about 255s.

Taking the 3^{th} sub-vehicle as an example, the sliding mode curves of three-channels with respect to the flight time are shown in Fig. 9(a) and (b), where the sliding mode surfaces s_1 and s_2 (see Equations (22) and (25)) of the 3^{th} sub-vehicle both converge to near zero with small oscillation induced by the external disturbances. Moreover, the acceleration curves of three-channels for the 3^{th} sub-vehicle are shown in Fig. 9(c), where the axial acceleration and lateral acceleration reach around zero while the normal acceleration finally converges to near the gravitational acceleration of projectile body.

5.3 Simulation results of Case 3

In this section, choose the observer gains in Equation (48) as follows: $\lambda_0 = 2, \lambda_1 = 3, \lambda_2 = 5, \delta = 30$; The control parameters in Equation (47) can be designed as follows: $k_0 = 0.03$, $t_r = 341.5$s, $n = 2$, $\eta = 5$, and the dynamic lag time constant of the autopilot is consistent with

https://doi.org/10.1017/aer.2021.30 Published online by Cambridge University Press

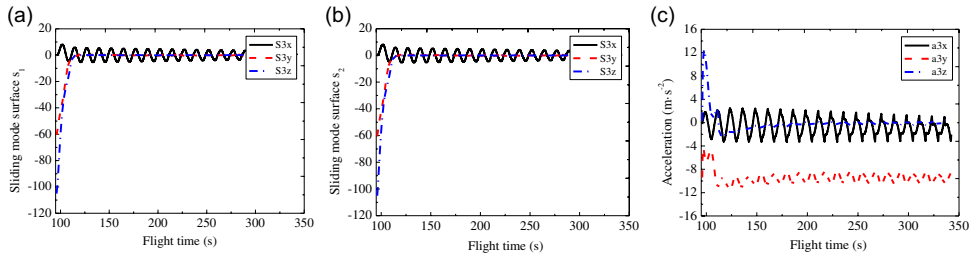

Sliding mode surface s_1 with respect to time

Sliding mode surface s_2 with respect to time

Acceleration with respect to time

Figure 9. Sliding mode surfaces and accelerations of the third sub-vehicle.

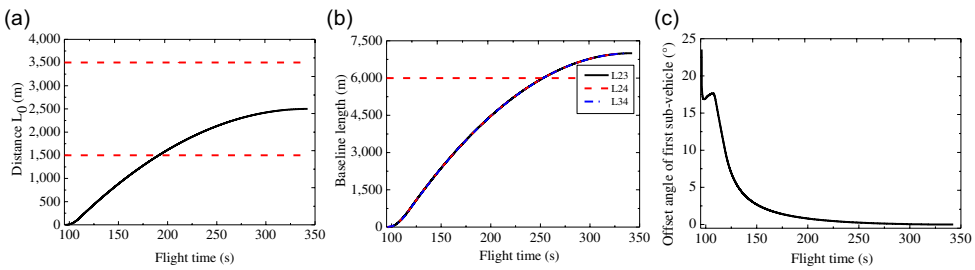

Relative distance L_0 with respect to time

Baseline length L_{23}, L_{24}, L_{34} with respect to time

Offset angle $\Delta center$ with respect to time

Figure 10. Configuration parameter curves with respect to time.

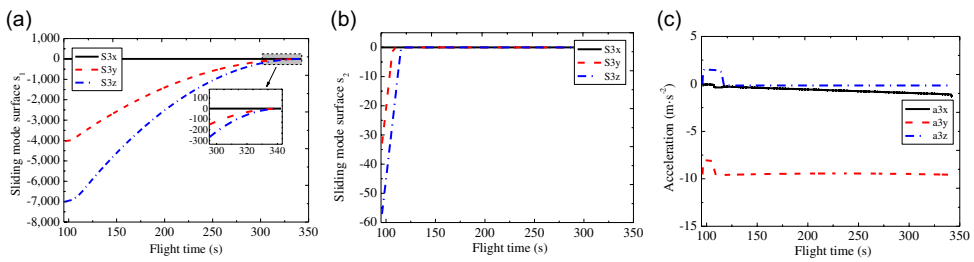

Sliding mode surface s_1 with respect to time

Sliding mode surface s_2 with respect to time

Acceleration with respect to time

Figure 11. Sliding mode surfaces and accelerations of the third sub-vehicle.

Case 2. In this case, the configuration parameters changing curves with respect to the flight time under the control law (44) are shown in Fig. 10. From Fig. 10, it can be seen that the formation configuration of the system converges at the desired time t_r, and the control law proposed in the Section 4.3 has high control precision.

To compare with Case 2, for the 3^{th} sub-vehicle, the sliding mode curves of three-channels with respect to the flight time are shown in Fig. 11(a) and (b), where the small-amplitude chattering is completely eliminated. The acceleration curves of three-channels for the 3^{th} sub-vehicle are shown in Fig. 11(c), where the acceleration responses are smaller than those shown in Fig. 9(c) and without chattering.

https://doi.org/10.1017/aer.2021.30 Published online by Cambridge University Press

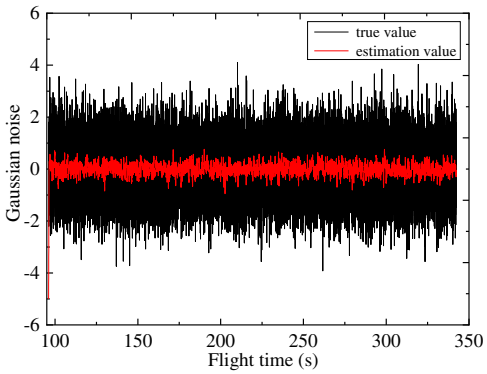

Figure 12. Gaussian white noise and estimation value.

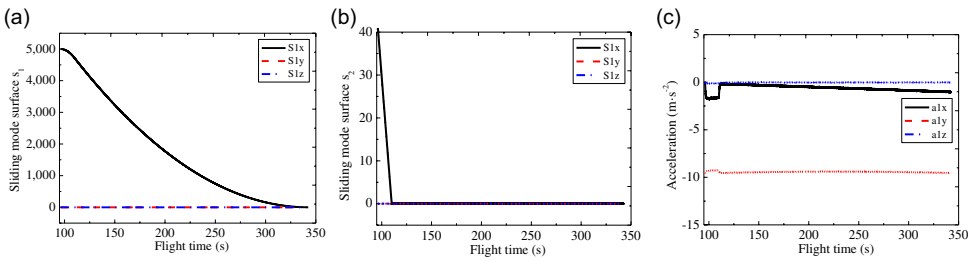

Sliding mode surface s_1 with respect to time

Sliding mode surface s_2 with respect to time

Acceleration with respect to time

Figure. 13. Sliding mode surfaces and accelerations of the first sub-vehicle.

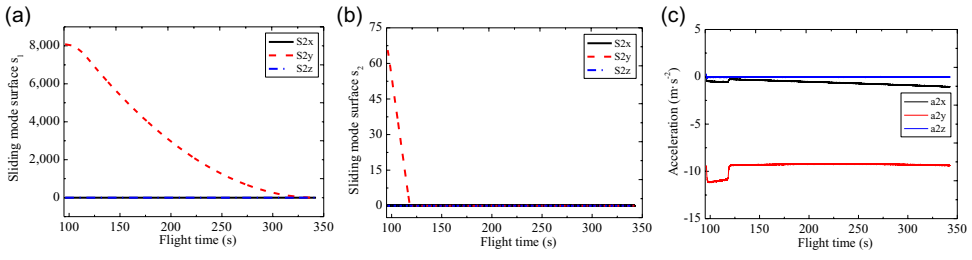

Sliding mode surface s_1 with respect to time

Sliding mode surface s_2 with respect to time

Acceleration with respect to time

Figure 14. Sliding mode surfaces and accelerations of the second sub-vehicle.

To further verify the effectiveness of proposed control law, next considering the Gaussian white noise disturbance shown in Fig. 12. For the sliding mode disturbance observer shown in Equation (48), the observer gains are still unchanged. The estimation of the noise is also given after passing through a first-order low pass filter, as shown in Fig. 12.

Under the effect of Gaussian noise, the control parameters in Equation (47) remain the same. For the formation system, the sliding mode curves and acceleration curves of three-channels with respect to the flight time are shown in Fig. 13, 14, 15 and 16. It is obvious that

https://doi.org/10.1017/aer.2021.30 Published online by Cambridge University Press

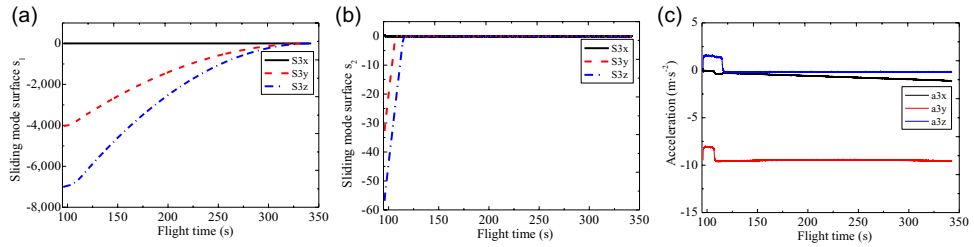

Sliding mode surface s_1 with respect to time

Sliding mode surface s_2 with respect to time

Acceleration with respect to time

Figure 15. Sliding mode surfaces and accelerations of the third sub-vehicle.

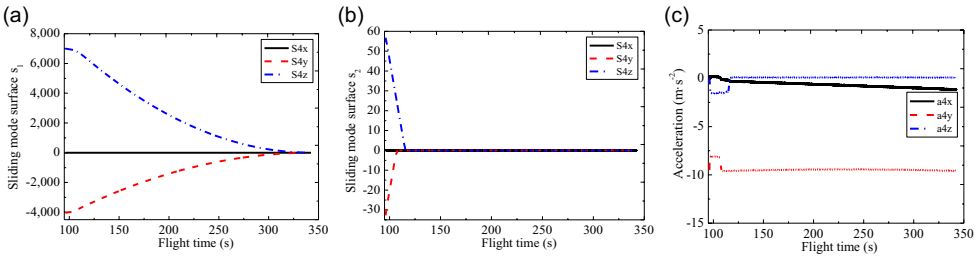

Sliding mode surface s_1 with respect to time

Sliding mode surface s_2 with respect to time

Acceleration with respect to time

Figure 16. Sliding mode surfaces and accelerations of the fourth sub-vehicle.

for the Gaussian white noise disturbance, the sliding mode surfaces s_1 (see Equation (22)) still converges to zero at the expected time, which means that the four sub-vehicles can form the expected formation configuration. Besides, for the sliding mode surfaces s_2 (see Equation (40)) and accelerations, they all converge in a finite time and the chattering is effectively suppressed during the flight.

6.0 CONCLUSION

In this paper, the cooperative control problem of space formation configuration for four reentry vehicles equipped with radar detector is researched during the mid-guidance phase. The expected position vector of each sub-vehicle is designed firstly according to the configuration constraints proposed based on a specific flight scenario. The adaptive second-order sliding mode controller is designed with considering the external disturbance and system noise, and the first-order dynamic characteristic of the autopilot. The conclusions of the investigations in this paper are listed as follows.

(1) The formation controlling errors can simultaneously converge to the neighbor of zero in a finite time, which means that the configuration constraints can be met effectively under the effect of the external disturbance and system noise.

(2) The maximum required acceleration for each sub-vehicle is reduced, and the chattering phenomenon of the sliding surfaces and the acceleration responses can be effectively suppressed, which is of great significance in engineering.

https://doi.org/10.1017/aer.2021.30 Published online by Cambridge University Press

DATA AVAILABILITY

The data used to support the findings of this study are available from the corresponding author upon request.

CONFLICTS OF INTEREST

The authors declare that there is no conflict of interests regarding the publication of this paper.

REFERENCES

1. WANG, X., ZHANG, Y. and WU, H. Distributed cooperative guidance of multiple anti-ship missiles with arbitrary impact angle constraint, *Aerosp Sci Technol*, 2015, **46**, (Oct.–Nov.), pp 299–311.
2. SHAFERMAN, V. and SHIMA, T. Cooperative differential games guidance laws for imposing a relative intercept angle, *J Guid Cont Dyn*, 2017, **40**, (10), pp 1–16.
3. WANG, X. and LU, X. Three-dimensional impact angle constrained distributed guidance law design for cooperative attacks, ISA Trans, 2018, **73**, pp 79–90.
4. LI, B., LIN, D.F. and WANG, H. Finite time convergence cooperative guidance law based on graph theory, *Optik - Int J Light Electron Opt*, 2016, **127**, pp 10180–10188.
5. SABOL, C., BURNS, R. and MCLAUGHLIN, C.A. Satellite formation flying design and evolution, J Spacecr Rockets, 2001, **38**, (2), pp 270–275.
6. REN, W. and BEARD, R.W. A decentralized scheme for spacecraft formation flying via the virtual structure approach, Proceedings of the American Control Conference, 2003.
7. NAZARI, M., BUTCHER, E.A., YUCELEN, T. and SANYAL YUCELEN, A.K. Decentralized consensus control of a rigid-body spacecraft formation with communication delay, *J Guid Cont Dyn*. A Publication of the American Institute of Aeronautics and Astronautics Devoted to the Technology of Dynamics and Control, 2016, **39**, (4), pp 838–851.
8. GHOMMAM, J., LUQUE-VEGA, L.F., *et al.* Three-dimensional distributed tracking control for multiple quadrotor helicopters, *J Franklin Inst*, 2016, **353**, (10), pp 2344–2372.
9. DONG, X., ZHOU, Y., REN, Z., *et al.* Time-varying formation tracking for second-order multi-agent systems subjected to switching topologies with application to quadrotor formation flying, *IEEE Trans Ind Electron*, 2017, **64**, (6), pp 5014–5024.
10. GHOMMAM, J., MEHRJERDI, H., MNIF, F., *et al.* Cascade design for formation control of nonholonomic systems in chained form, *J Franklin Inst*, 2011, **348**, (6), pp 973–998.
11. TAI, F., ZHAO, X.X., *et al.* Ultraviolet anti-collision and localization algorithm in UAV formation network – Science direct, *Optik*, 2019, **192**, p 162919.
12. HUANG, J. and SUN, W. A method of feasible trajectory planning for UAV formation based on bi-directional fast search tree. *Optik - Int J Light Electron Opt*, 2020, **221**, pp 165213.
13. CUI, N.G., WEI, C.Z., GUO, J.F. and ZHAO, B. Research on missile formation control system, Proceedings of IEEE International Conference on Mechatronics and Automation, 2009, pp 4197–4202.
14. REZAEE, H. and ABDOLLAHI, F., Motion synchronization in unmanned aircrafts formation control with communication delays, *Commun Nonlinear Sci Numer Simul*, 2013, **18**, (3), pp 744–756.
15. WEI, C.Z., GUO, J.F., LU, B.G., SHI, Y. and ZHANG, L.B. Adaptive control for missile formation keeping under leader information unavailability, Proceedings of IEEE International Conference on Control and Automation, 2013, pp 902–907.
16. WANG, X.F., LIU, D.Z., TIAN, Z. A composite formation strategy for multiple missile, Proceedings of IEEE International Conference on Control, Automation and Robotics, 2017, pp 684–691.
17. WEI, C.Z., SHEN, Y., MA, X.X., GUO, J.F. and CUI, N.G. Optimal formation keeping control in missile cooperative engagement, *Aircr Eng Aerosp Technol* 2012, **84**, (6), pp 376–389.
18. ZHAO, E.J., CHAO, T, WANG, S.Y., *et al.* Finite-time formation control for multiple flight vehicles with accurate linearization model. *Aerosp Sci Technol*, 2017, **71**, pp 90–98.
19. RATNOO, A. and SHIMA, T. Formation-flying guidance for cooperative radar deception. *J Guid Cont Dyn*, 2012, **35**, (6), pp 1730–1739.

https://doi.org/10.1017/aer.2021.30 Published online by Cambridge University Press

20. WANG, H., GUO, D., LIANG, X., *et al.* Adaptive vision-based leader-follower formation control of mobile robots. IEEE Trans Ind Electron, 2017, **64**, (4), pp 2893–2902.
21. NAN, W. and JIEQIONG, X. Leader-follower formation control of networked spacecraft in deep space, 2nd International Conference on Advanced Computer Control, IEEE, Shenyang, China, 2010, pp 527–530.
22. YU, S., YU, X., SHIRINZADEH, B., *et al.* Continuous finitetime control for robotic manipulators with terminal sliding mode, *Automatica*, 2005, **41**, (11), pp 1957–1964.
23. HARL, N. and BALAKRISHNAN, S. Impact time and angle guidance with sliding mode control, *IEEE Trans Cont Syst Technol*, 2012, **20**, (6), pp 1436–1449.
24. LEVANT, A. Higher-order sliding modes, differentiation, and out-feedback control, Int J Cont, 2003, **76**, (9/10), pp 924–941.

https://doi.org/10.1017/aer.2021.30 Published online by Cambridge University Press